Title: Influence of Branched Ligand Architectures on Nanoparticle Interactions with Lipid Bilayers

Authors: Carlos A. Huang-Zhu[1], Reid C. Van Lehn[1,2]

[1]Department of Chemical and Biological Engineering, University of Wisconsin−Madison, Madison, Wisconsin 53706, United States

[2]Department of Chemistry, University of Wisconsin−Madison, Madison, Wisconsin 53706, United States

Keywords: molecular dynamics, nanoparticles, ligand chain architecture, free energy, bilayer adsorption

ABSTRACT

Gold nanoparticles functionalized with organic cationic ligands have shown promise as biomedical agents, but their interactions with cellular membranes are not yet well-understood and design rules for ligands that promote desired cellular interactions are lacking. Past experimental studies have demonstrated that ligand lipophilicity, quantified by the ligand end group partition coefficients, can be used as a descriptor for predicting nano–bio interactions, but such a descriptor is incapable accounting for ligand architecture, such as chain branching. To probe the effects of ligand end architecture on ligand-lipid interactions, we perform molecular dynamics simulations to investigate how ligand alkyl chain branching modulates thermodynamics and mechanisms of nanoparticle adsorption to lipid membranes. We designed four pairs of 2 nm diameter gold nanoparticles where each pair had ligand end groups with similar lipophilicity but varying alkyl chain architecture (*e.g.*, one long alkyl chain vs two short chains) to isolate branching effects from lipophilicity. Free energy calculations and mechanistic insight revealed that alkyl end group branching can decrease free energy barriers for adsorption by disrupting ligand monolayer packing, increasing end group protrusions that lead to favorable ligand intercalation with minimal membrane disruption. Furthermore, increased end group branching promotes adsorption by increasing the exposure of nonpolar surface area to water, which results in a greater reduction of free energy upon exposure to the nonpolar core of the lipid bilayer. These results show that ligand chain architecture can modulate nano–bio interactions, limiting the exclusive use of lipophilicity as a sole descriptor to predict cellular uptake of surface-functionalized nanoparticles.

INTRODUCTION

Surface-functionalized nanoparticles (NPs) have become a valuable tool for biomedical applications.[1–3] These materials possess highly tunable physicochemical properties that make them versatile materials for applications such as antibacterial treatments[4], therapeutics[5], diagnostics[5], disease prevention[6], photothermal therapy[7], and drug delivery[8]. In these applications, the interactions of NPs with cellular membranes are critical in determining their efficacy and safety, motivating interest in design criteria that impact NP-membrane interactions. For example, experimental studies have shown that tuning NP size, shape, and surface chemistry can significantly influence nano–bio interactions such as cellular entry.[9–11] Recent advances have been made to increase cellular uptake, in particular, by functionalizing NP surfaces with organic ligands that can modulate their interactions with the cell membrane.[12,13] However, the nano–bio interactions that drive cellular entry can also lead to adverse behaviors such as cytotoxicity and hemolysis, hindering the utility of these nanomaterials for biomedical applications and inhibiting clinical translation.[14,15] These challenges have motivated efforts to design NPs that can enter cells with minimal cytotoxicity.[9,12] Although parametric studies have shown that cellular internalization is dependent on NP core material[10,11], size[9,16,17], shape[16,18], surface charge[9,11,19], and ligand lipophilicity[10] (log *P*), pathways and mechanisms for cellular entry remain under active study.

Within the large design space of nanomaterials, gold nanoparticles (AuNPs) coated with a self-assembled monolayer of amphiphilic ligands have been shown to exhibit high cellular uptake, biocompatibility, and versatility.[9,20,21] These amphiphilic ligands possess tunable lipophilic and charged groups that interact with lipid tails and head groups, respectively, making ligand-functionalized AuNPs promising biomedical agents and excellent platform materials to elucidate nano–bio interactions.[22–24] However, the design space of potential ligand structures – even when restricted to amphiphilic ligands – remains challenging to explore experimentally due to the expense and time associated with AuNP synthesis and *in vitro* cellular entry assays. Consequently, methods are needed to predict interactions between ligand-functionalized AuNPs and biological membranes prior to synthesis.

As a step toward predicting ligand-mediated nano-bio interactions, Rotello and co-workers have identified log *P* as a ligand-specific descriptor that can be easily evaluated prior to synthesis and correlates with AuNP interactions.[12,13,15,25,26] Ligand log *P* is a measure of lipophilicity that describes how strongly (or weakly) the ligands favor the hydrophobic core of lipid bilayers; larger values of log *P* indicates a stronger preference for partitioning into hydrophobic environments. For example, AuNPs coated with zwitterionic ligands were shown to generally exhibit higher cellular uptake for ligands with higher log *P* in the absence of serum proteins.[12] The same set of AuNPs, however, showed a nonmonotonic trend in the presence of serum proteins, where the least and most lipophilic ligands showed the highest uptake.[12] More defined nonmonotonic trends have also been observed for cationic ligands with uncharged alkyl moieties as end groups.[13] However, ligand-functionalized AuNPs with end groups composed of alcohols, cyclic structures, or branches exhibit weaker correlations between cellular uptake and log *P*.[13,15,26,27] In general, these studies have demonstrated that ligand log *P* can describe nano–bio interactions to some extent, but there are still outliers that are yet to be explained, such as ligands with branched alkyl end groups.[13,15,26]

Additionally, the lack of mechanistic insight further minimizes the feasibility of exclusively relating log *P* to nano–bio interactions *a priori*.

To better understand how physicochemical properties of ligands modulate nano–bio interactions, computational modeling has been employed to predict NP surface properties from the interplay of interactions between self-assembled ligands[28,29], and to elucidate thermodynamic and mechanistic insight on NP-bilayer interactions.[30–51] Recent work in our group has focused on studying the relationship between log *P* and the quasi-irreversible adsorption of AuNPs coated with a cationic ligand monolayer to zwitterionic lipid bilayers.[30,31] This cationic ligand is composed of (1) a 1-undecanethiol hydrophobic backbone, (2) a tetraethylene glycol (PEG) chain for biocompatibility, and (3) a cationic quaternary ammonium (TTMA) with a tunable R group that modulates nano–bio interactions. The tunable R group is of great importance as it has been shown by the Rotello group that its lipophilicity (*i.e.*, log *P*) can regulate cellular uptake, cytotoxicity, hemolysis, and protein corona formation[1,8,12,13,21]. We performed coarse-grained (CG) molecular dynamics simulations to study the adsorption of AuNPs to zwitterionic lipid bilayers for a series of AuNPs with ligands of varying log *P*.[30] We demonstrated that combining the distance between the AuNP and bilayer and the number of contacts between ligands and lipids provides an appropriate reaction coordinate to describe AuNP adsorption. We further found that ligand R group log *P* is nonmonotonically related to the free energy barrier for adsorption by dictating whether adsorption occurs through ligands favorably intercalating into the lipid bilayer or lipid tails unfavorably protruding out of the bilayer. These results indicate that single-ligand descriptors, such as log *P*, can lead to incomplete predictions of NP-membrane interactions. However, this past study, as well as related literature on nano–bio interactions[31,35–37,52–57], has focused on ligands with linear architectures, neglecting more complex chain architectures that may lead to significantly different nano–bio interactions.

In this work, we sought to explore the hypothesis that chain architecture will affect AuNP adsorption for ligands with similar values of log *P* by perturbing the interplay of ligand–ligand and ligand–lipid interactions that was found to determine adsorption thermodynamics and mechanisms in our past work.[30] To do so, we expanded the library of AuNPs studied in past work[30] by systematically designing four pairs of AuNPs coated with ligands of similar log *P* but different chain architecture (*i.e.*, alkyl R group branching) as shown in Figure 1. All ligand architectures are based on the same structure developed by Rotello and co-workers to ensure experimental relevance[13,15]. Three pairs consist of a linear and either a double-branched or triple-branched R group, while the most lipophilic pair consists of a double-branched and a triple-branched R group. Throughout the rest of this manuscript, we will refer to the linear 11-Carbon (11-C), 15-Carbon (15-C), 19-Carbon (19-C), and double-branched 27-Carbon (27-C) as the lower-branched R groups, while the double-branched 11-C, triple-branched 15-C, double-branched 19-C, and triple-branched 27-C will be referred to as the higher-branched R groups. We employed CG simulations using the string method with swarms of trajectories[30,58–60] and path variables[30,61] to simulate the adsorption of a single AuNP to a zwitterionic 1,2-dilinoleoyl-sn-glycero-3-phosphocoline (DIPC) bilayer – which is a CG representation of the more common 1,2-dioleoyl-sn-glycero-3-phosphocoline DOPC bilayer – as a function of the distance between the AuNP and the bilayer and the number of ligand–lipid contacts.[30] We show that similarly lipophilic ligands with different

chain architectures exhibit different thermodynamics and mechanisms for adsorption to DIPC bilayers. Increasing the number of alkyl R group branches, while keeping a fixed number of hydrophobic beads (representing carbon atoms), decreases the average free energy barrier for adsorption. We attribute this behavior to increased alkyl R group protrusions that promote favorable lipophilic contacts with the lipid tails while minimizing membrane disruption (*e.g.*, mechanisms associated with lipid extraction, such as lipid tails protruding out of the bilayer). We also show that increased alkyl R group branching substantially decreases adsorption free energies due to a greater decrease in surface area exposure to water that is mediated by increased exposure to the nonpolar environment of the membrane core. Both results emerge from the disruption of packing due to the branched groups. These findings reveal striking and nonintuitive behaviors for nano–bio interactions that cannot be predicted from log *P* alone, indicating the importance of alternative ligand design criteria when considering the molecular design and engineering of nanomaterials for biomedical applications.

RESULTS AND DISCUSSION

Minimum free energy pathway yields reaction coordinate for potential of mean force calculation

To probe the effects of ligand R group branching on the thermodynamics for adsorption, we computed the potential of mean force (PMF) for AuNP adsorption to DIPC bilayers as a function of the distance along the minimum free energy path (MFEP), as described in our previous study[30]. The MFEP represents the most energetically favorable (*i.e.*, most probable) path for NP adsorption to the lipid bilayer. Free energy calculations along this transition pathway yield the free energy barrier that the NP must cross to initiate the adsorption process. We described the MFEP using two CVs: the center-of-mass distance between the AuNP and the bilayer projected onto the *z*-axis normal to the membrane (D_z; note that this is computed using a scaled value, $\widetilde{D}_z$, as discussed in the Methods), and the number of ligand–lipid contacts (N_c). To compute the MFEP, we solvated a single AuNP near a bilayer (representative snapshot shown in Figure 1C) and used the string method with swarms of trajectories[30,58–60] to iteratively evolve an initial string toward the MFEP. A spline fit of the last five converged strings was defined as the MFEP using path variables[30,61] and was discretized for umbrella sampling as a function of the distance of the path (*S*). Additional details are provided in the Methods section and a schematic of this workflow is shown in Figure S1.

We computed four estimates of the MFEP from separate replicas (Figures S2-S13) to relate states along the reaction coordinate with the thermodynamics and mechanisms of AuNP adsorption. To illustrate these calculations, Figure 2A shows a schematic of representative states sampled as the CVs change along the MFEP in addition to MFEPs computed for one replica of the 15-C ligand pair with representative simulation snapshots. All MFEPs are included in the SI (Figures S2-S13). The normalized distance along the MFEP (*S*) is represented by the color map in Figures 2B and 2C. For both linear (Figure 2B) and branched (Figure 2C) ligands, the number of ligand–lipid contacts, N_c, is zero when the AuNP is far from the bilayer (large D_z), as illustrated in (i) in Figure 2A. This state corresponds to small values of *S.* Following the MFEP (increasing *S*) leads to a decrease in D_z and, as the AuNP approaches the bilayer, an increase in N_c, as represented in state (ii) in Figure 2A. Qualitatively, MFEPs for the linear and branched ligands show distinct

differences during the initial interaction with the bilayer associated with state (ii). As observed by comparing Figures 2B and 2C, the MFEP for the linear ligand shows a steep increase in N_c at approximately D_z = 5.60 nm whereas the branched ligand instead shows a gradual increase at approximately D_z = 6.10 nm. This trend is consistently observed for linear and branched ligand R groups, indicating distinct mechanisms of adsorption, and is further discussed below. Figures S14-S21 show these regions of interest zoomed-in for clarity. The initial increase in N_c between ligands and lipids associated with this region leads into the transition state where the AuNP must overcome an energetic barrier (further discussed below) to initiate adsorption that is dependent on the ligand alkyl R group and its interaction with the bilayer as observed from the simulation snapshots in Figure 2B and 2C. Following the transition state, increasing *S* toward values close to 1 leads to a decrease in D_z with an increase in N_c that corresponds to NP adsorption and lipid extraction from the bilayer, as depicted in state (iii) in Figure 2A.

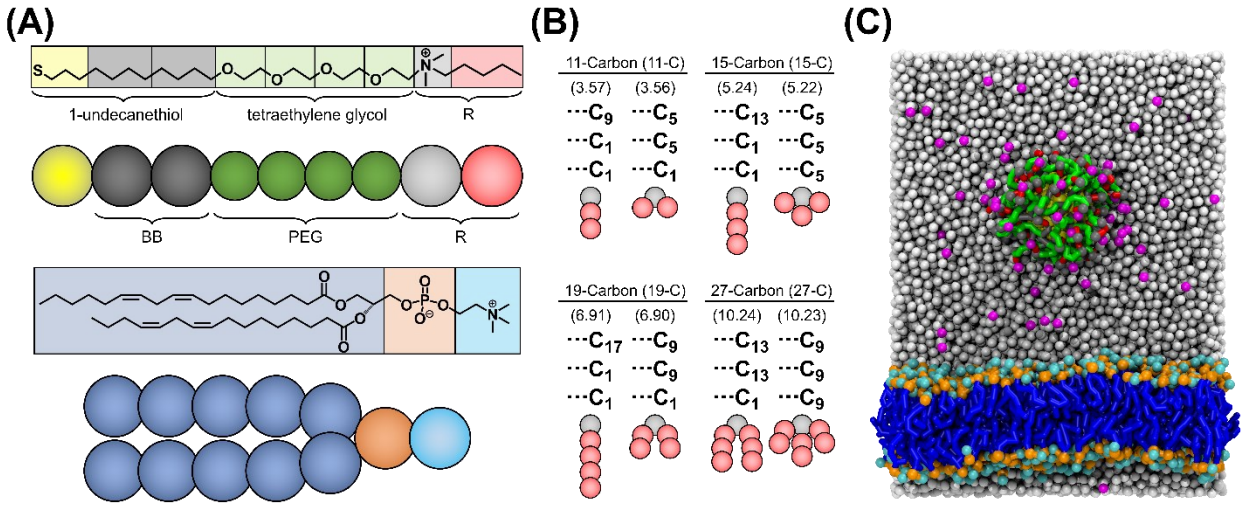

Figure 1. Summary of systems studied. (A) Chemical structures and CG models of the cationic ligand and DIPC lipids. The R group consists of the TTMA cation (bead mapping includes only three carbon atoms) and the additional carbon atoms of the branches. (B) Library of R groups studied (labels do not include the hydrogen atoms). Log *P* values of the R groups are shown in parentheses and were extracted from ChemDraw version 21.0.0 using Crippen's method[62]. Log *P* for the 27-Carbon pair was estimated by cumulative contributions of single carbons since ChemDraw was unable to compute these values. (C) Representative snapshot of the initial configurations for the solvated AuNPs. The colors for the AuNP and the DIPC lipids follow (A); BB and TTMA are the same shade of grey, but the latter is represented as a sphere for visual purposes. Water beads are white and Cl^- counterions are magenta. Half of the water beads are not shown for clarity. All simulations snapshots were rendered using Visual Molecular Dynamics[63].

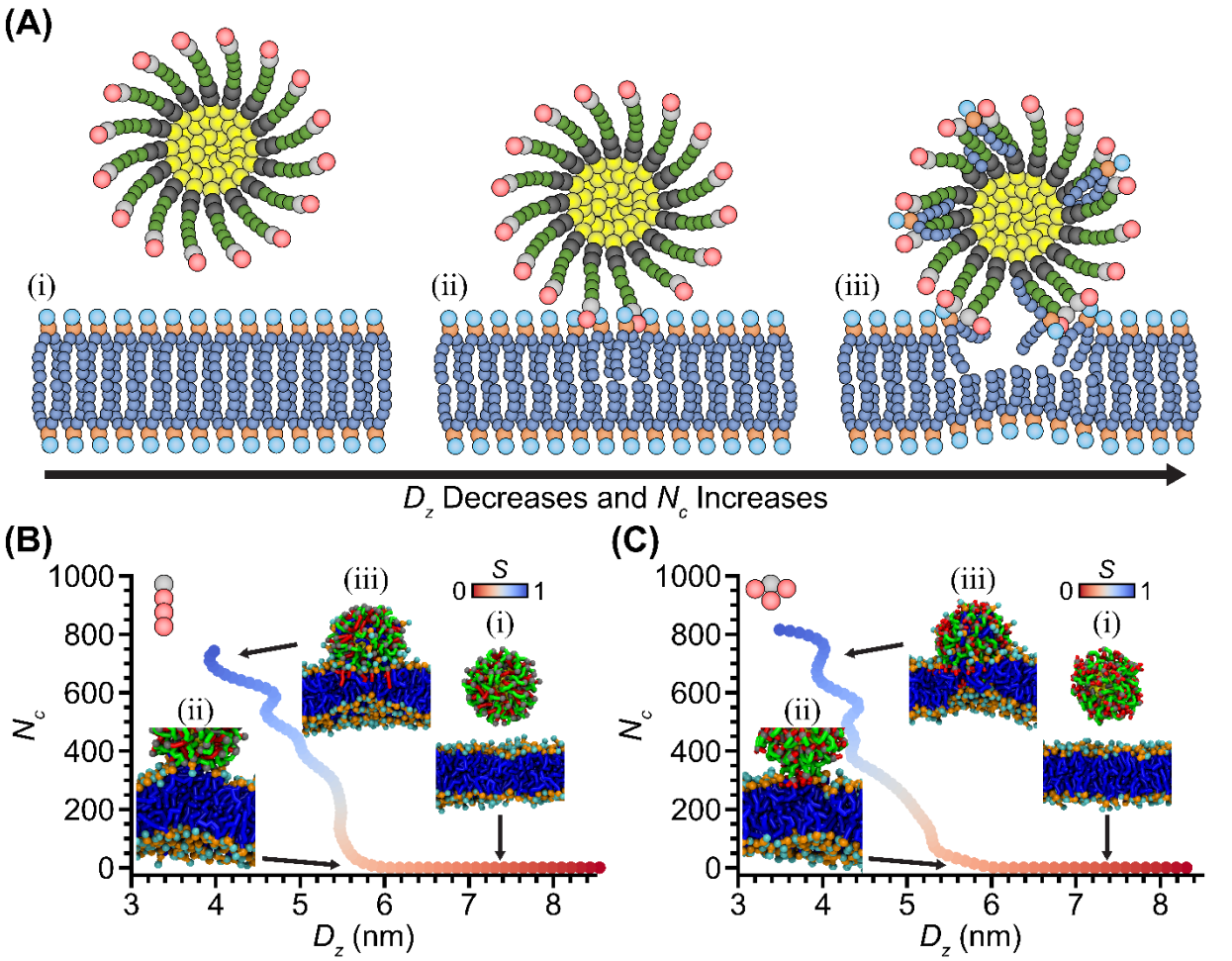

Figure 2. Calculation of minimum free energy paths (MFEPs) for 15-C ligand pair. (A) Schematic of AuNP adsorption to lipid bilayers described in CV space. States (i) to (iii) schematically indicate key states in the MFEPs and correspond to the similarly labeled simulation snapshots. (B) MFEP for one replica of the linear 15-C ligand alkyl R group. (C) MFEP for one replica of the triple-branched 15-C ligand alkyl R group. The color map for the MFEPs corresponds to the normalized distance along the path (S). Representative simulation snapshots were taken from the last five strings that were used to fit the spline. All water beads, counterions, and lipids in the bilayer that are in front of the NP were removed for visual purposes. Colors follow Figure 1.

Next, we computed the PMF as a function of S. Since each MFEP differs in CV space from one another, S was normalized by its largest value for each replica to ensure $0 \leq S \leq 1$ in all cases. We defined the free energy barrier for adsorption as the largest PMF difference between the first maximum and the first minimum (PMF Max.), and the adsorption free energy as the global free energy minimum (PMF Min.). The PMFs in Figure 3 show that all AuNPs exhibit well-defined free energy barriers at $0.25 < S < 0.45$, ranging from 10.5 k_BT to 22.8 k_BT (13.0 k_BT to 21.4 k_BT when averaged across replicas, depending on the ligand R group). Furthermore, all AuNPs show strong irreversible adsorption with free energies of adsorption between -175.3 k_BT and -20.6 k_BT

(-161.6 k_BT to -30.3 k_BT when averaged across replicas, depending upon the ligand R group). We discuss in detail the free energy barriers for adsorption and the adsorption free energies in the following sections. Qualitative observations for the PMFs between each pair of ligands reveal that replicas of higher-branched ligands (solid lines) generally exhibit a sharp free energy barrier (single peak) that is shifted to lower values of *S*, whereas lower-branched ligands (dashed lines) show wider free energy barriers (broader peak). Higher-branched ligands also lead to lower adsorption free energies on average with PMFs that exhibit similar and more consistent features, as opposed to the PMFs of the lower-branched counterparts that show more deviations between replicas. These observations can be correlated to more variation in umbrella sampling near the free energy barrier for adsorption where ligands with linear alkyl R groups have more windows with similar D_z, but vary in N_c, whereas ligands with branched alkyl R groups will have less variation (Figures S14-S21). The sharp PMF increases observed at large *S* for some replicas are attributed to sampling small values of D_z and large values of N_c that can lead to subsequent transition pathways for full NP insertion into the bilayer bulk (*i.e.*, several ligands interacting with the opposite leaflet of the bilayer). However, in-depth analysis of those high free energy states is out of the scope of this manuscript and will be investigated in future work.

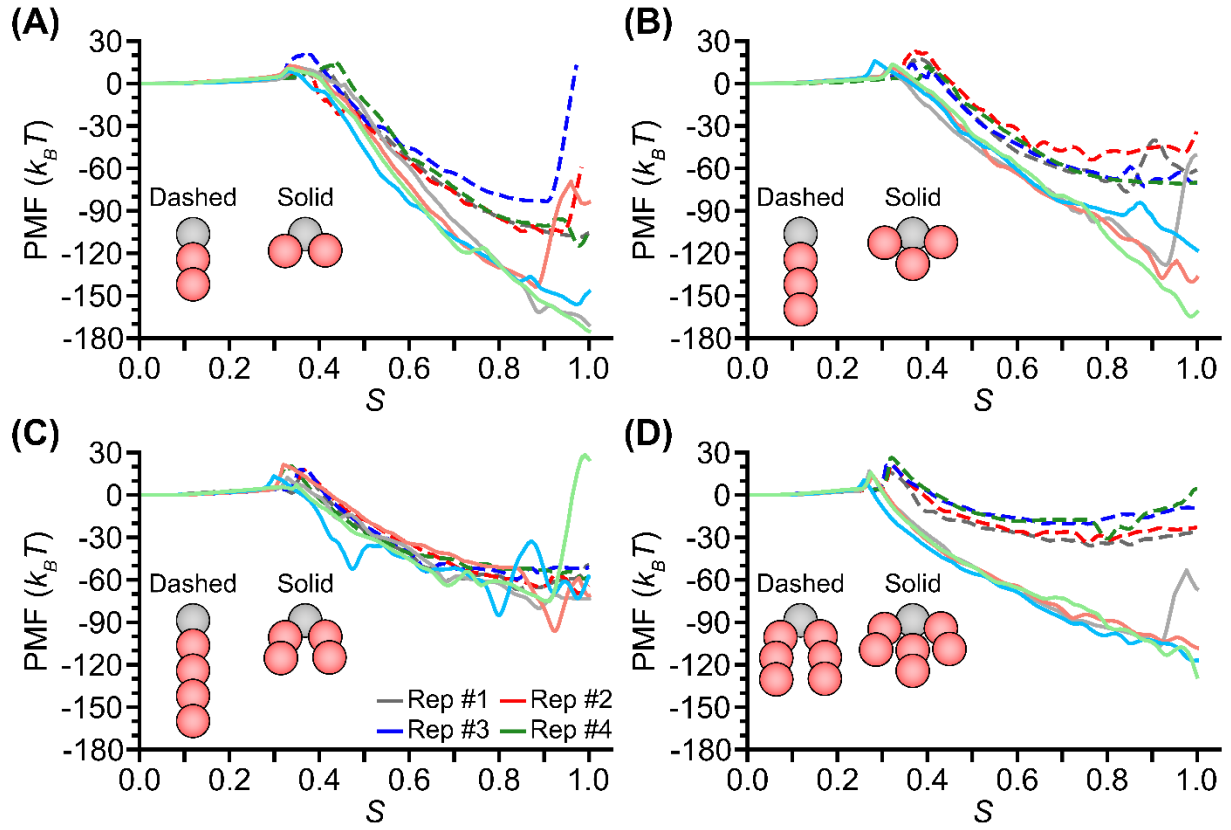

Figure 3. Potentials of mean force (PMF) computed along the MFEPs for: (A) 11-Carbon pair, (B) 15-Carbon pair, (C) 19-Carbon pair, (D) 27-Carbon pair. Dashed curves correspond to lower-branched alkyl R groups and solid curves correspond to higher-branched alkyl R groups. Each curve corresponds to a single replica (four replicas per ligand). PMF values for small *S*, corresponding to the NP in solution far from the bilayer, were set to 0 k_BT for all replicas.

Branched R groups affect mechanisms of bilayer adsorption

To quantify the effects that branching has on adsorption thermodynamics and mechanisms, Figure 4 compares free energy barriers for adsorption (PMF Max.) for pairs of ligands with equal log *P* values but different degrees of branching. For each AuNP, we show the replica free energy barriers (white circles) and the mean free energy barrier (gray diamonds). Although replica values show moderate spread in some cases, the mean values are consistently lower for higher-branched alkyl R groups with standard deviations between replicas within 1.6 k_BT and 5.9 k_BT. Upon further inspection of the replica MFEPs (Figures S14-S21), we attribute these deviations to slight differences in CV values for each replica. Particularly, for higher-branched alkyl R groups, replicas that show a higher free energy barrier follow an early transition state where ligand–lipid contacts are initiated at larger D_z (*i.e.*, when the NP is farther away from the bilayer) whereas lower barriers are observed when contacts are initiated at smaller D_z (*i.e.*, when the NP is closer to the bilayer). Additionally, CV values calculated for the window near where the free energy barriers are observed show that linear R groups generally exhibit a larger number of ligand–lipid contacts (Figures S14-S21). The data altogether show that, as branching of the alkyl R group increases, the free energy barrier decreases and is shifted to smaller *S* compared to the equivalent lower-branched ligands, which corresponds to an increase in N_c at larger D_z. These observations suggest that chain architecture modulates NP adsorption and ligand–lipid contacts through nonintuitive mechanisms.

We inspected representative snapshots from umbrella sampling windows close to where the free energy barriers were observed to identify mechanistic pathways for adsorption. In our previous works, we identified three mechanisms for adsorption in which ligand R group log *P* determines whether adsorption occurs through favorable ligand intercalation into the bilayer or unfavorable lipid tail protrusions.[30,31] Ligands with short and slightly lipophilic (*i.e.*, small log *P*) R groups require unfavorable lipid tail protrusions out of the bilayer (*i.e.*, stochastic protrusion out of the bilayer hydrophobic bulk into solution) due to the inability of short ligand alkyl chains to protrude out of the ligand monolayer (*i.e.*, stochastic protrusion out of the ligand monolayer into solution) to initiate ligand–lipid contacts. On the contrary, alkyl R groups of medium chain length and moderate lipophilicity can protrude out of the ligand monolayer to initiate contacts, minimizing unfavorable lipid tail protrusions by favorably intercalating within the bilayer. However, long and highly lipophilic ligand alkyl chains result in R groups strongly backfolding back into the ligand monolayer (*i.e.*, R groups remain partitioned within the hydrophobic core of the ligand monolayer), preventing R group protrusions, and then requiring unfavorable lipid tail protrusions to initiate NP adsorption. These mechanisms led to a nonmonotonic trend in free energy barriers to adsorption with log *P*. Based on these findings, we sought to compare our previous results to the previously identified mechanisms.

The representative snapshots in Figure 4 show that the least lipophilic AuNPs (11-C) adsorb to the bilayer through ligand intercalation (*i.e.*, red R groups intercalate into the bilayer) with mean barriers of $14.6 \pm 4.4\ k_BT$ for the linear R group and $10.9 \pm 1.6\ k_BT$ for the double-branched alkyl R group. In the case of AuNPs with intermediate lipophilicities (15-C and 19-C), we observed strikingly different adsorption mechanisms between linear and branched alkyl R groups. The AuNPs with linear ligands adsorb through backfolding lipid tail protrusions, where the R group

strongly backfolds into the ligand monolayer requiring unfavorable lipid tail protrusions to initiate adsorption (*i.e.*, blue lipid tail groups extend into the AuNP monolayer) with mean barriers of 16.4 ± 4.8 k_BT and 17.4 ± 3.1 k_BT, for the 15-C and 19-C AuNPs, respectively. However, their branched counterparts adsorbed through more favorable ligand intercalation with lower mean barriers of 13.0 ± 2.3 k_BT and 13.6 ± 5.9 k_BT, respectively. Although these are positive free energy barriers, the decreased barrier height along with the observation of ligand intercalation is in agreement with our previous conclusions that ligand intercalation is more favorable than lipid tail protrusions due to lower membrane disruption.[30] Finally, the most lipophilic AuNPs (27-C) adsorb through a previously unseen, fusion-like mechanism with a mean barrier of 21.4 ± 4.7 k_BT for the double-branched alkyl R group, and 14.2 ± 2.8 k_BT for the triple-branched alkyl R group. This mechanism consists of ligand R groups not fully protruding due to moderate backfolding but instead being highly exposed to the membrane due to steric effects induced by the branched chain architectures. This exposure, in conjunction with the inability for ligands to intercalate into the bilayer, results in the formation of a lipid bridge[30] formed by the alkyl R group branches and the lipid tails at the AuNP-membrane interface. This state is similar to the lipid mixing observed during vesicle-vesicle fusion and is stabilized by (1) electrostatic attraction between the ligand TTMA groups and lipid phosphate groups, and (2) lipophilic contacts between ligand alkyl R groups and lipid tails.

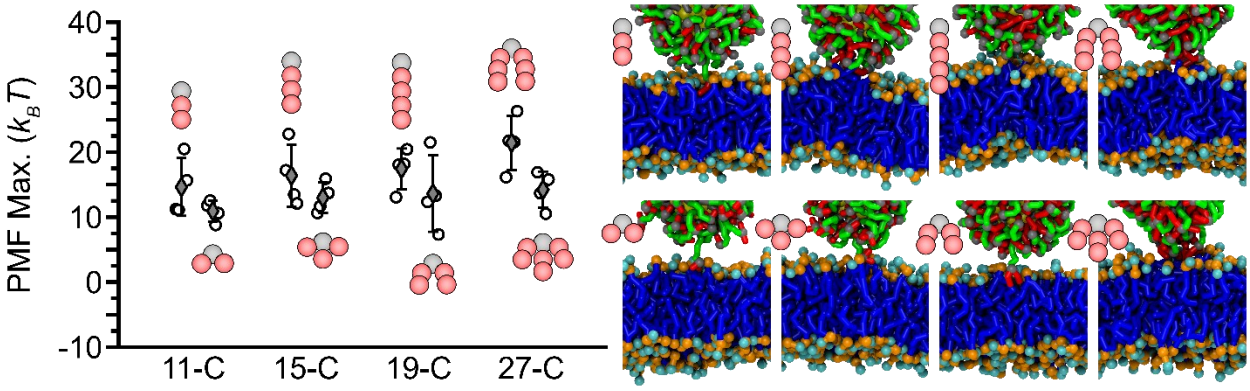

Figure 4. Free energy barriers for adsorption (PMF Max.). The plot shows replica values as white circles and the mean values as gray diamonds. Error was computed as the standard deviation between four replicas. Simulation snapshots were taken from the replica with the free energy barrier closest to the mean value, and from windows close to where the barrier is observed (in *S*). All water and counterions, and lipids in the bilayer that are in front of the AuNP were removed for visual purposes. Colors follow Figure 1.

Protrusions increase exposure of lipophilic ligand R groups

The simulation snapshots in Figure 4 suggest that ligand branching promotes the intercalation of ligands, motivating analysis of radial distribution functions (RDFs) to quantify the extent to which this behavior can be related to ligand protrusions into solution even when far from the bialyer.[30] In Figure 5 we computed the RDFs for the ligand TTMA and R groups and show that higher-branched ligands protrude into solution more than their lower-branched counterparts. To quantify the number of beads that protrude out of the ligand monolayer, we used the radius of the RDF peak

corresponding to the ligand TTMA (r_{TTMA}) as a reference cut-off distance. For the single RDF showing a binodal distribution (*i.e.*, triple-branched 27-C), we used the mean radius instead. Comparing the RDFs of the R groups and TTMA groups suggests that a number of R group beads lie at the same radial distance as that of the TTMA or farther away, indicating R group protrusions out of the ligand monolayer and into solution where they would be available to interact with the bilayer. We integrated the RDF of R groups for $r > r_{TTMA}$ (Table S2) and found that the number of beads that protrude for higher branched ligands is approximately 5×, 82×, 10×, and 5× higher for the 11-C, 15-C, 19-C, and 27-C ligand R groups, respectively. The AuNPs with ligand R groups of intermediate lipophilicities (15-C and 19-C) show the largest increase in protrusions upon increasing the number of branches, correlating with the change in adsorption mechanism during initial NP–bilayer contact observed in Figure 4. Specifically, linear architectures for 15-C and 19-C ligand R groups require unfavorable lipid tail protrusions because strong R group backfolding limits intercalation into the bilayer. However, changing the chain architecture by increasing the number of branches and decreasing the branch chain length weakens R group backfolding, increasing protrusions out of the ligand monolayer that permit favorable ligand intercalation. In contrast, the 11-C and 27-C ligands show only a 5× increase in protrusions out of the ligand monolayer for the branched alkyl R groups, but the mechanistic pathway remains the same as the lower-branched counterparts. These results are thus in agreement with the free energy calculations and qualitative observations from simulation snapshots, further indicating that R group protrusions out of the ligand monolayer at the AuNP–bilayer interface promote intercalation for ligands terminated with lipophilic alkyl R groups.

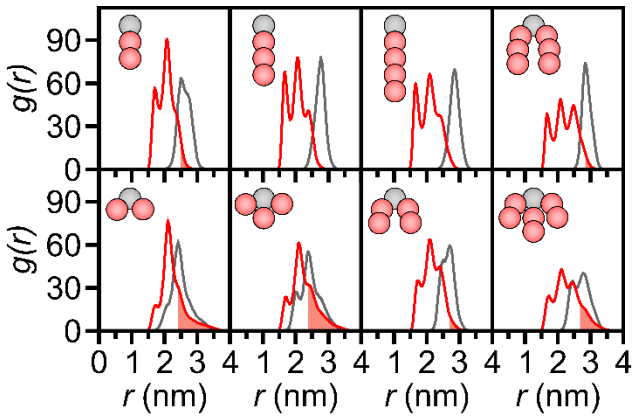

Figure 5. Radial distribution functions (RDFs) for TTMA and R groups. Error was computed as the standard deviation between three replicas. Integrals of the red shaded area under the curve are calculated in Table S2. Curves are color coded as the included schematic of the R groups (same as in Figure 1). The *gmx rdf* tool was used with a bin size of 0.01 nm to calculate *g(r)*.

Ligand–lipid contacts relative to hydrophilic contacts provide insight into membrane disruption.

We next sought to formulate a quantitative metric that can provide characteristic insight on NP–bilayer interactions. Specifically, we rationalized that hydrophilic contacts due to strong electrostatic attraction between the ligand TTMA and the lipid phosphate groups must be present after initial lipophilic contacts between ligand R groups and lipid tails are established, such that

comparing the balance of hydrophilic *vs.* lipophilic contacts could provide insight into interactions that impact adsorption free energy barriers. Therefore, in Figure 6 we computed $\widehat{N}_c$ as the contacts between lipid tails and different ligand groups (*i.e.*, hydrophobic backbone, PEG chains, and R groups) normalized by the number of hydrophilic contacts. These relative ligand–lipid contacts were calculated for the trajectory corresponding to the umbrella sampling window closest to where the free energy barrier was observed. Only groups lower than 1 nm below the center of mass of the AuNP and lipids within a cylinder with a 3 nm radius centered around the center of mass of the AuNP were considered for the calculation. These strict cut-offs restricted the calculation to only lipids at the AuNP–bilayer interface and excludes lipids that may have been extracted.

Figure 6 reveals that for all pairs of AuNPs, the backbone and PEG groups of the lower-branched ligands come into contact with lipid tails (positive BB and PEG values of $\widehat{N}_c$). For the linear 11-C ligand R group, these contacts are present because the intercalated ligand can pull the NP close to bilayer without extracting lipids or causing lipid tails to unfavorably protrude out of the bilayer. This observation is in agreement with the less steep MFEP and earlier onset of contacts slightly farther away from the bilayer as observed in the MFEPs in Figures S14-S21. For the linear 15-C and 19-C ligand R groups, the larger number of relative contacts for backbone and PEG chains is associated with lipid tails protruding out of the bilayer because the longer alkyl chains strongly backfold into the ligand monolayer. In contrast, the double-branched 27-C ligand R group has very few relative contacts with the backbone and PEG chains, but significantly more relative contacts with R groups. However, visualization of the umbrella sampling trajectories revealed that in one of the replicas, a lipid bridge was formed, but later relaxed by extracting a single lipid. The lipid extraction process thus produced the low number of relative contacts with the core groups of the ligand monolayer. For the rest of the trajectories, states alternate between semi-fusion through a lipid bridge, and ligand intercalation, suggesting that this alternating behavior could lead to slightly higher than expected free energy barriers for the double-branched 27-C ligand R group in Figure 4.

Surprisingly, none of the higher branched counterparts show any lipid contacts with the backbone and PEG chains of the ligands. For the higher-branched 11-C, 15-C, and 19-C ligand R groups, this correlates to ligands fully intercalating into the bilayer, which minimizes lipid tail protrusions that can reach the ligand backbone and PEG groups within the ligand monolayer. For both double- and triple-branched 27-C ligand R groups (after accounting for the single lipid extraction event), the large number of lipid relative contacts are due to the lipid bridge that stabilizes the semi-fused state. The much larger relative contacts for the triple-branched 27-C ligand R group are in agreement with visual inspection of the trajectories. As observed in the corresponding simulation snapshot from Figure 4, the lipid bridge appears to be more pronounced with slightly more R groups extended and in contact with more lipid tails due to more lateral displacement of lipids that exposes the hydrophobic bulk of the bilayer.

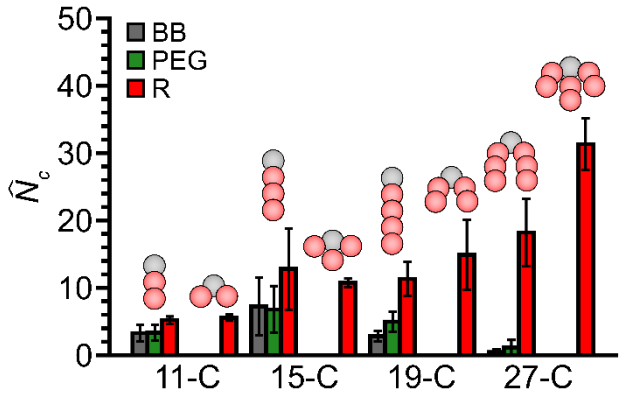

Figure 6. Contacts between ligand groups and lipid tails normalized by the number of hydrophilic contacts between ligand TTMA and lipid phosphate groups. Contacts were defined using a cut-off distance of 0.705 nm, corresponding to 1.5 × 0.47 nm (standard diameter of a MARTINI bead). Error was computed as the standard error between four replicas.

These data show that lipophilic contacts between NP–grafted ligands and lipids play an important role in NP adsorption to lipid bilayers. In particular, increased branching of ligand alkyl R groups reduces lipid tail contacts with the backbone and PEG chains of ligands by minimizing bilayer–disrupting lipid tail protrusions and lipid extraction. At the same time, lipophilic contacts between the ligand R groups and lipid tails either remain high or increase by promoting favorable NP–bilayer interactions. Therefore, the trends observed with the lipid relative contacts further support our hypothesis that branched ligand alkyl R groups can lower free energy barriers for adsorption by promoting favorable ligand intercalation that minimizes membrane disruption.

Branched R groups substantially increases thermodynamic stability of adsorbed AuNPs

Having established the effect of branching on mechanisms underlying the onset of adsorption to the bilayer, corresponding to state (ii) in Figure 2A, we next compared adsorption free energies to determine the effect of branching on the thermodynamics of adsorption, corresponding to state (iii) in Figure 2A. Figure 7 shows values of PMF Min. which are equivalent to adsorption free energies. Comparing values between the higher-branched ligands and the lower-branched ligands reveals that within pairs of ligands of similar log *P*, increased branching of the ligand alkyl R group lowers the adsorption free energy by 20.4 k_BT up to 85.0 k_BT when averaged across replicas, depending upon the ligand R group. The linear 11-C and 15-C R groups have mean adsorption free energies of -103.0±13.5 k_BT and -68.6±10.0 k_BT, respectively, while their double-branched and triple-branched counterparts have mean adsorption free energies of -161.6 ± 14.3 k_BT and -137.9 ± 20.2 k_BT, respectively. At very high log *P*, the double-branched 27-C ligand has a mean adsorption free energy of -30.3 ± 6.9 k_BT, while the triple-branched has a mean adsorption free energy of -115.3 ± 9.9 k_BT. Overall, the higher-branched R groups for these three pairs of ligands have over 50% lower adsorption free energies when compared to their lower-branched counterparts. The substantially lower adsorption free energies for the higher-branched ligands indicate that AuNPs functionalized with branched alkyl R groups adsorb more strongly to lipid bilayers in comparison to R groups with fewer branches despite similar log *P* values.

The adsorption free energies along with the simulation snapshots show that branching leads to a significantly different adsorbed state at large values of *S* that reflects the change in adsorption free energy. The simulation snapshots in Figure 7 reveal that AuNPs functionalized with the lower-branched ligands (top row) are stably bound to the outer leaflet of the bilayer. In this state, lipids are extracted into the ligand monolayer and ligands have their lipophilic R groups partition into the bilayer due to attractive interactions with lipid tails. However, for the higher-branched ligands, the AuNPs assume configurations in which the charged groups of the ligands fully cross the membrane and are now bound to the opposite leaflet, acting like "anchors", with their R groups partitioning towards the hydrophobic core of the bilayer and preventing the AuNP from desorbing. Such states, where AuNP-grafted ligands are distributed between both leaflets, have been identified to be metastable for negatively charged ligands[37,57,64,65]. On the contrary, the linear and branched 19-C ligands show the smallest difference in adsorption free energy (-20.4 k_BT) with mean values of -63.8 ± 5.2 k_BT and -84.2 ± 9.1 k_BT, respectively. In this case, both AuNPs remain stably bound to the upper leaflet without any ligands having crossed the membrane core. Figure 7 thus shows that a change in chain architecture of alkyl R groups can lead to substantially increased AuNP adsorption and corresponding mechanistic changes. Furthermore, observing such favorable adsorption free energies for AuNPs in a partially inserted state suggests that these NPs should exhibit increased cellular entry, in line with prior experimental observations[9].

Finally, Figure 7 also shows that increasing log *P* for either linear or branched ligand R groups increases the adsorption free energies (*i.e.*, more positive PMF Min.), which might seem counterintuitive as increased R group lipophilicity would be expected to increase favorable interactions with the hydrophobic lipid tails and thus decrease adsorption free energies. We attribute this trend to an interplay between the free volume of the ligand monolayer and lipid extraction. Shorter, less lipophilic R groups are exposed to water prior to adsorption, resulting in a large free volume within the ligand monolayer that also exposes hydrophobic ligand backbones to water; this behavior is more pronounced for branched ligands, as further discussed below. Upon adsorption, lipid extraction into the ligand monolayer permits hydrophobic interactions between lipid tails and ligand backbones to promote a highly favorable adsorption free energy. Increasing R group lipophilicity (log *P*), however, leads to R group backfolding into the ligand monolayer prior to adsorption due to hydrophobic interactions between the ligand R group and ligand backbones. Backfolding decreases the free volume with the ligand monolayer, and consequently adsorption is less favorable since lipid extraction is reduced and leads to fewer new hydrophobic interactions with ligand backbones. These observations further reinforce our hypothesis that R group lipophilicity alone is insufficient to capture the complex set of ligand-ligand, ligand-lipid, and ligand-water interactions that collectively determine the thermodynamics of adsorption.

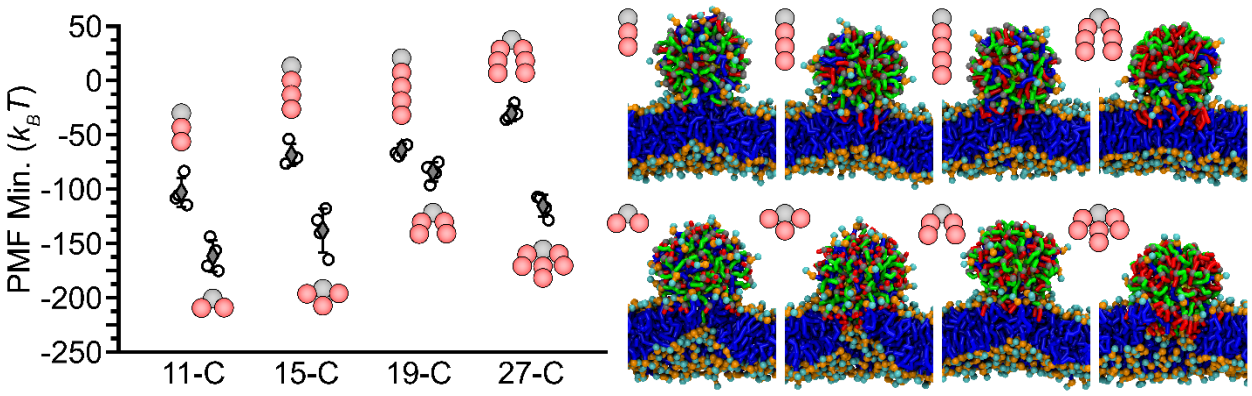

Figure 7. Adsorption free energies (PMF Min.). The plot shows replica values as white circles and mean values as gray diamonds. Error was computed as the standard deviation between four replicas. Simulation snapshots were taken from the replica with the adsorption free energy closest to the mean value, and from windows close to where the global free energy minimum is observed (as a function of *S*). All water beads, counterions, and lipids in the bilayer that are in front of the AuNP were removed for visual purposes. Colors follow Figure 1.

Surface exposure of lipophilic R groups influences adsorption free energies

We further investigated how ligand alkyl R group branching promotes adsorption by computing the solvent–accessible surface area (SASA) for the R group lipophilic beads of the AuNPs in solution and in a fully adsorbed state. We hypothesized that branching induces a steric effect that increases exposure of lipophilic groups to water, introducing a free energy penalty that is eliminated upon AuNP adsorption because this nonpolar surface area can be sequestered within the nonpolar environment of the membrane core. This hydrophobic driving force would be consistent with previous studies that show that lipophilic contacts are one of the main driving forces for NP adsorption to lipid bilayers[30,31,36,37] and ligand-receptor binding[66,67]. We thus computed the R group SASA for each pair of AuNPs in solution and for the AuNPs in the fully adsorbed state using the umbrella sampling trajectories corresponding to the adsorption free energies in Figure 7 to determine how R groups lead to a reduced SASA due to adsorption to the bilayer or lipid extraction.

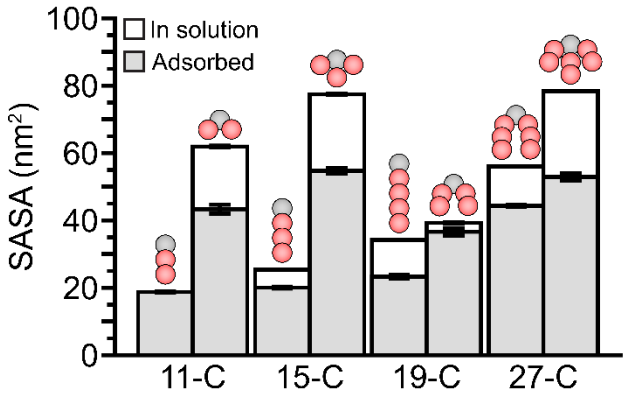

Figure 8. Decrease in R group solvent-accessible surface area (SASA) upon AuNP adsorption to lipid bilayers. The SASA was computed only for the lipophilic beads of the R groups. White bars correspond to the SASA calculated for AuNPs solvated in water without a bilayer. Grey bars correspond to the SASA calculated for AuNPs adsorbed to the bilayer using the trajectories from umbrella windows close to where the global free energy minimum is observed (as a function of *S*). SASA for the adsorbed 11-C linear R group AuNP overlaps the SASA of the AuNP in solution by 0.83 nm^2. Error was computed as the standard error between three replicas for the AuNPs in solution and between four replicas for the AuNPs adsorbed to the bilayer. The *gmx sasa*[68] tool was used to calculate the SASA with a probe radius of 0.26 nm and 4800 grid points.

Figure 8 shows that trends in the SASA for each pair of AuNPs in solution (white bars) agree with the trends observed for protrusions in Figure 5 and Table S2; the higher-branched 11-C, 15-C, and 27-C R groups show significantly larger SASA than their lower-branched counterparts just as these exhibit significantly more protrusions. The difference in SASA between the linear and branched 19-C R group pair is minimal and this pair also exhibits the fewest protrusions. For AuNPs in their adsorbed state, these overall trends generally remain the same with higher-branched ligands having higher SASA. Comparing the difference in SASA between AuNPs in the solution and adsorbed states for each ligand pair generally shows that at fixed log *P*, the relative difference in SASA between lower- and higher-branched R groups agree with trends in the adsorption free energies in Figure 7. Lower-branched R groups exhibit a smaller decrease in SASA when transitioning from the solution to adsorbed states and have less favorable (less negative) adsorption free energies, whereas higher-branched R groups have a larger decrease in SASA when transition from solution to adsorbed states and have more favorable (more negative) adsorption free energies. Therefore, large relative changes in SASA between AuNPs in solution and adsorbed to the bilayers, as well as higher absolute SASA, are indicative of lower adsorption free energies, reflecting the hydrophobic driving force discussed above. We attribute this behavior primarily to the disruption of packing in the ligand monolayer by higher-branched R groups, which increases the SASA in solution and decreases the SASA upon adsorption by both promoting lipid extraction to shield exposed nonpolar surface area in the ligand monolayer and sequestering a large number of R groups within the hydrophobic core of the bilayer. The apparent exception is the 19-C R group pair, which has a small decrease in SASA for both the linear and branched groups and correspondingly similar adsorption free energies.

Ligands with branched R groups exhibit lipid-like behaviors

The effects of alkyl chain architecture that we have described are consistent with similar studies based on structure-activity relationships between linear and branched alkyl moieties in a variety of contexts. For example, branching leads to increased stability for ligand-functionalized nanocrystals[69], higher dispersibility of metal-oxide nanoparticles in hydrophobic solvents[70], more potent antifungal activity for alkyl gallates[71], improved intracellular delivery of mRNA-lipid nanoparticles[72], and superior power conversion for small molecule-based organic solar cells[73]. Although these previous reports are based on other classes of materials, the main conclusion that chain architecture modulates different functions can be generalized to the NP–bilayer interactions studied here.

Perhaps most relevant are observations on the effect of branching on the properties of lipids through both computational[74] and experimental[72] methods. Shinoda and colleagues used MD simulations to compare DPPC and DPhPC lipid bilayers, where the latter only differs from the former by having four additional methyl groups as side chains in each tail.[74] They concluded that lipid tail branching in DPhPC bilayers disrupts lipid packing, but increases bilayer stability due to the entrapment of lipid tails between neighboring lipids. More recently, Hashiba and colleagues systematically studied the effects of lipid tail symmetry and total carbon number in lipid nanoparticles for mRNA delivery.[72] Through hemolysis assays, they discovered that increased packing disruption due to tail branching promotes endosomal escape. Similarly, in the AuNPs studied in this work, branching minimizes backfolding of ligand alkyl R groups by disrupting ligand monolayer packing (analogous to lipid packing in bilayers). Similar packing disruption increase the exposure of lipophilic groups to lipid tails through ligand intercalation, thus decreasing free energy barriers for adsorption. In analogy to lipid properties that influence bilayer structure, this comparison suggests avenues for exploring alternative variations to ligand properties, such as varying the degree of ligand saturation of bulkiness, to further disrupt monolayer packing as a means of influencing bilayer interactions.

CONCLUSIONS

In this work, we employed coarse-grained (CG) molecular dynamics simulations using the MARTINI force field to elucidate the thermodynamics and mechanisms of AuNP adsorption to zwitterionic DIPC lipid bilayers by expanding upon our previous computational framework[30]. to study AuNPs. We systematically studied a library of AuNPs grafted with cationic ligands and terminated with alkyl R groups in which we determined the effects of alkyl R group branching by selecting four pairs of R groups in which each pair had R groups of similar log *P* (*i.e.*, number of hydrophobic beads) but with different chain architectures (*i.e.*, number of alkyl branches). We show that, within pairs of AuNPs with ligands of similar log *P*, increased ligand alkyl R group branching reduces free energy barriers for adsorption. The branched chain architectures inhibit R group packing (backfolding) within the ligand monolayer and increase protrusions into solution. This effect alters the mechanism for adsorption by promoting favorable ligand intercalation within the bilayer, which minimizes bilayer disruption. Moreover, we show that for highly lipophilic and branched R groups, adsorption proceeds through a fusion-like mechanism where a lipid bridge forms at the AuNP–bilayer interface. For the same pairs of AuNPs, increased branching also leads

to significantly more favorable adsorption free energies. The higher number of branches leads to an increased unfavorable exposure of nonpolar R groups to water, incurring in a free energy penalty. Adsorption to the lipid bilayer eliminates this energetic penalty as the R groups instead sequester nonpolar surface area within the membrane core.

This study provides significant and valuable insight into the effects that alkyl R group chain architecture of NP–grafted ligands can have on NP–bilayer interactions and show that using log *P* as a sole descriptor for AuNP adsorption to lipid bilayers may not be sufficient to predict cellular interactions. The impact of branching suggests design rules that can be leveraged in the engineering of nanomaterials for biomedical applications to improve cellular uptake and intracellular delivery while minimizing undesired membrane disruption that can lead to adverse effects such as cytotoxicity and hemolysis. Finally, an unexpected observation is that AuNPs with branched ligands can achieve partially inserted states in which some ligand charged groups cross the hydrophobic core of the bilayer to interact with the opposite leaflet even though the barrier for the crossing of a single charged ligand is approximately 10 k_BT in AA simulations[52] and 16[37] to 30[35] k_BT in CG simulations. Although the reaction coordinate we employ to describe adsorption does not capture free energy barriers for these crossing events, their observation suggests that these are energetically favorable configurations seemingly facilitated by the disruption of lipid tail packing within the membrane core by branched R groups. Future work will explore the thermodynamics of such ligand translocation processes to determine if branching can be employed to achieve direct AuNP translocation across the bilayer.

METHODS

Simulation parameters

All coarse-grained simulations were performed with GROMACS 2021.5[75] patched with PLUMED 2.8.0[76]. Interactions were described using the MARTINI force field (version 2.3P[77,78]) with the refined polarizable water model[79,80]. Molecular dynamics simulations were performed using a leapfrog integrator with a 20 fs timestep. The temperature was kept constant at 300 K using a velocity-rescale thermostat with a 1.0 ps time constant. The pressure was kept constant at 1 bar with semi-isotropic pressure coupling and a compressibility of 3×10^{-4} bar^{-1} in both the *xy* and *z* directions. Systems were first energy-minimized using the steepest descents method for 5,000 steps or until the maximum force was less than 1,000 kJ mol^{-1} nm^{-1}. During equilibration simulations (*vide infra*), a Berendsen barostat with a coupling constant of 5.0 ps^{-1} was used. A total of 45 ns of equilibration was performed for unbiased simulations of the AuNPs solvated in water far from the bilayer. The equilibrated systems were then used as initial configurations for the calculation of the MFEPs. During production simulations, a Parrinello-Rahman barostat with a coupling constant of 12.0 ps^{-1} was used. AuNP bonds that yielded force constants greater than 15,000 kJ mol^{-1} nm^{-2} during parameterization were constrained using the LINCS algorithm with an order of 4 for stability. Van der Waals interactions were modeled using a Lennard-Jones interaction with the potential smoothly shifted to zero at a cutoff distance of 1.1 nm. Neighbor lists were generated using the Verlet algorithm with a cut-off of 1.1 nm. Electrostatic interactions were modeled using the smooth Particle Mesh Ewald algorithm with a short-range cut-off of 1.1 nm, a

spacing of 0.12 nm for the Fourier grid, and a dielectric constant of 2.5. These interaction parameters are all consistent with MARTINI recommendations[77–80].

Description of systems

Solvated zwitterionic bilayers were generated using the *insane.py* script[81] with initial system dimensions of 14 nm × 14 nm × 24 nm and contained a total of 578 DIPC lipids and ~30,000 water beads (using the polarizable water model). System neutrality was achieved by adding 72 Cl^- counterions. Table S1 contains the exact number of water molecules for each system.

The AuNPs were modeled using 72 ligands, as shown in Figure 1, with the grafting density based on experimental data[9]. Ligands were arranged spherically to form a hollow shell with a diameter of 2 nm following our prior work[30,55,56]. From the 1-undecanethiol segment, the $S(CH_2)_3$ group was modeled as a C5 bead in MARTINI, while the $(CH_2)_4$ groups were modeled as C1 beads. The tetraethylene glycol groups were modeled using four ethylene oxide (EO) beads developed by Grunewald et al.[82]. The quaternary ammonium (TTMA) group was modeled as a Q0 bead representing a choline group in which the carbons are not shared with the R groups. Although we refer to the positively charged group as a quaternary ammonium, the actual CG bead mapping consists of three carbon atoms instead of four to ensure a 4:1 mapping for the 1-undecanethiol and correct restructuring of branched chain architectures, which was only possible by mapping the EO bead as [$O\text{-}CH_2\text{-}CH_2$] instead of the original [$CH_2\text{-}O\text{-}CH_2$]. Each R group bead represents four carbon atoms.

Each AuNP was individually parameterized based on all-atom (AA) simulations through a bottom-up approach to capture conformational effects that arise from ligand grafting to the AuNP surface.[30] Simulations of the AuNPs at the AA scale used the CHARMM36[83] force field. Distributions of the bond lengths and angles were used to calculate the CG bonded parameters. The C5 beads that compose the hollow shell were bonded to their nearest C5 neighbors within 1.24 nm using a harmonic potential with a spring constant of 5,000 kJ mol^{-1} nm^{-2} to obtain a stable and rigid core. Specific details regarding this bottom-up parameterization can be found in our previous work[30].

Definition of collective variables

The reaction coordinate for free energy calculations was described using two CVs: $\widetilde{D}_z$ and N_c. We defined $\widetilde{D}_z$ as the scaled distance (with respect to the z-component of the simulation box) between the center of mass of the AuNP and the center of mass of the bilayer projected onto the z-axis normal to the membrane. The center of mass of the bilayer was computed using 20 randomly selected lipids (10 lipids from each leaflet). We chose to use the scaled distance to minimize numerical instabilities that may originate from bilayer deformations during steered MD simulations and umbrella sampling. However, we plot all data using the unscaled distance (D_z, which has units of nm) for improved interpretability (Figures 2, S2-S21, and S54-S57). To calculate D_z, we multiplied $\widetilde{D}_z$ by either the z-component of the simulation box averaged from the final configurations of the 24 restrained windows of the last five strings, or the time-averaged z-component of the simulation box of each umbrella trajectory. For free energy calculations, a contact, N_c, was defined as one bead found within 0.47 nm of another bead (*i.e.*, any AuNP bead

with respect to any lipid bead) following the standard size of MARTINI beads. The DISTANCE and COORDINATION collective variables implemented in PLUMED 2.8.0[76] were used to compute $\widetilde{D}_z$ and N_c, respectively.

String method with swarms of trajectories

We computed the minimum free energy paths (MFEPs) using the string method with swarms of trajectories[30,58–60]. Following our previous work[30], the initial string was defined between two equilibrium states: the AuNP in solution far from the bilayer, and the AuNP adsorbed to the upper leaflet of the bilayer, as shown in (i) and (iii) in Figure 2A. Configurations for the initial string were obtained from two steered-MD simulations. During the first, $\widetilde{D}_z$was decreased from 0.41 to 0.16 at a rate of -0.01 ns^{-1} using a harmonic potential with a spring constant of 100,000 kJ mol^{-1} while N_c was retrained to 0 using a harmonic potential with a spring constant of 200 kJ mol^{-1} $contact^{-2}$. The final configuration from this simulation was used to initiate the second steered-MD simulation in which N_c was increased from 0 to 800 at a rate of 10 contacts ns^{-1} using a harmonic potential with a spring constant of 0.5 kJ mol^{-1} $contact^{-2}$ while $\widetilde{D}_z$ was restrained to 0.16 using a harmonic potential with a spring constant of 100,000 kJ mol^{-1}.

The initial string was composed of 24 total windows: 6 windows with decreasing $\widetilde{D}_z$ and N_c restrained to 0, and 18 windows with increasing N_c and $\widetilde{D}_z$ restrained to 0.16.[30,58] The evolution of the initial string was completed after 75 iterations. For all windows, each iteration began with a 0.2 ns simulation in which $\widetilde{D}_z$ and N_c were restrained to their target values by harmonic potentials with spring constants of 100,000 kJ mol^{-1} and 0.5 kJ mol^{-1} $contact^{-2}$, respectively. A second 0.2 ns simulation was performed with the spring constants increased to 200,000 kJ mol^{-1} and 1 kJ mol^{-1} $contact^{-2}$. A third 0.2 ns simulation using the same restraints was performed as production from which 128 configurations were generated for each window. These 128 frames were used to initiate 24 swarms of unbiased simulations (*i.e.*, the swarms of trajectories), one per window.[30,58] Each unbiased simulation in the swarm was performed for 0.2 ps without restraints to sample the CVs. The drift of the CVs was averaged over all trajectories for each window and added to the old CVs to evolve the string. The new string was then reparameterized to ensure equal distances between consecutive windows. The strings obtained from the last five iterations were averaged in CV space and fitted with a spline to obtain the MFEP.[30,58] Evolutions of the strings are found in Figures S2-S9. All converged MFEPs in CV space are found in Figures S10-S13.

1D umbrella sampling

The MFEP was described using the path equations by Branduardi et al.[61] to define the distance along the path, *S*, and the normal distance away from the path, *Z*. The PATH collective variable implemented in PLUMED 2.8.0[76] was used to compute *S* and *Z*. The path was discretized into 72 windows equally spaced as a function of *S* for 1D umbrella sampling with initial configurations taken from the last five strings. Strong umbrella potentials were used for windows in which the AuNP begins generating contacts with the bilayer; these windows were slightly different across all ligands and across all replicas. Weak potentials were used for all other windows. To ensure exclusive sampling of the MFEP, an umbrella potential of 20,000,000 kJ mol^{-1} was used to restrain *Z* close to 0. All values for *S*, *Z*, and their restraints are included in the SI. All umbrella windows

were simulated for 50 ns. CV values computed from the umbrella sampling trajectories were compared to the MFEP and the five strings used for the spline fit to ensure that CV sampling from both methodologies were in agreement (Figures S14-S21). Convergence was assessed as described in the SI (Figures S22-S53). For ligands with linear R groups, the last 45 ns of the 50 ns simulations were used for analyses, and for ligands with branched R groups, the last 40 ns were used. Four fully independent strings and umbrella sampling calculations were performed for each AuNP to ensure the robustness of the results. For the linear ligand architectures, two of the four replicas were taken from our past work[30], while the other two replicas were newly simulated. The free energy as a function of *S* was computed using the Weighted Histogram Analysis Method (WHAM)[84].

CONFLICTS OF INTEREST

There are no conflicts to declare.

ACKNOWLEDGEMENTS

This material is based upon work supported by the National Science Foundation under grant No. DMR-2044997. C.A.H.-Z. and R.C.V.L. acknowledge the support provided by the Graduate Engineering Research Scholars−Advanced Opportunity Fellowship from the University of Wisconsin−Madison, the Chemistry-Biology Interface Training Program (T32GM152341), funded by the National Institute of General Medicine Sciences, from the University of Wisconsin−Madison, the National Science Foundation through a Graduate Research Fellowship. This work used resources from the Advanced Cyberinfrastructure Coordination Ecosystem: Services & Support (ACCESS), supported by the National Science Foundation under the Office of Advanced Cyberinfrastructure awards #2138259, #2138286, #2138307, #2137603 and #2138296.

SUPPLEMENTARY INFORMATION

The supplementary information includes a single PDF file with 57 figures, 2 tables, and additional information on the computational workflow, data supporting the convergence of simulation quantities, and additional data for replicas of the computational workflow.

DATA AVAILABILITY STATEMENT

The supplementary information includes GROMACS structure and topology files for the coarse-grained models of the NPs studied and a spreadsheet with information on all simulation conditions to facilitate reproducibility.

REFERENCES

1 R. Mout, D. F. Moyano, S. Rana and V. M. Rotello, *Chem. Soc. Rev.*, 2012, **41**, 2539–2544.

2 G. Sanità, B. Carrese and A. Lamberti, *Front. Mol. Biosci.*, 2020, **7**, 587012.

3 Y. Kumar, A. S. K. Sinha, K. D. P. Nigam, D. Dwivedi and J. S. Sangwai, *Nanoscale*, 2023, **15**, 6075–6104.

4 D. P. Linklater, X. Le Guével, G. Bryant, V. A. Baulin, E. Pereiro, P. G. T. Perera, J. V. Wandiyanto, S. Juodkazis and E. P. Ivanova, *ACS Appl. Mater. Interfaces*, 2022, **14**, 32634–32645.

5 S. Jiang, K. Y. Win, S. Liu, C. P. Teng, Y. Zheng and M.-Y. Han, *Nanoscale*, 2013, **5**, 3127–3148.

6 F. Ghaemi, A. Amiri, M. Y. Bajuri, N. Y. Yuhana and M. Ferrara, *Sustainable Cities and Society*, 2021, **72**, 103046.

7 N. Kim, Y.-G. Jeong, S. Lee, J. Kang, Y. Kim, Y.-A. Choi, D. Khang and S.-H. Kim, *ACS Appl. Mater. Interfaces*, 2024, **16**, 12217–12231.

8 R. Das, R. F. Landis, G. Y. Tonga, R. Cao-Milán, D. C. Luther and V. M. Rotello, *ACS Nano*, 2019, **13**, 229–235.

9 Y. Jiang, S. Huo, T. Mizuhara, R. Das, Y.-W. Lee, S. Hou, D. F. Moyano, B. Duncan, X.-J. Liang and V. M. Rotello, *ACS Nano*, 2015, **9**, 9986–9993.

10 X. Bai, S. Wang, X. Yan, H. Zhou, J. Zhan, S. Liu, V. K. Sharma, G. Jiang, H. Zhu and B. Yan, *ACS Nano*, 2020, **14**, 289–302.

11 Y. Xiao, W. Xu, Y. Komohara, Y. Fujiwara, H. Hirose, S. Futaki and T. Niidome, *ACS Omega*, 2020, **5**, 32744–32752.

12 D. F. Moyano, K. Saha, G. Prakash, B. Yan, H. Kong, M. Yazdani and V. M. Rotello, *ACS Nano*, 2014, **8**, 6748–6755.

13 K. Saha, M. Rahimi, M. Yazdani, S. T. Kim, D. F. Moyano, S. Hou, R. Das, R. Mout, F. Rezaee, M. Mahmoudi and V. M. Rotello, *ACS Nano*, 2016, **10**, 4421–4430.

14 C. M. Goodman, C. D. McCusker, T. Yilmaz and V. M. Rotello, *Bioconjugate Chem.*, 2004, **15**, 897–900.

15 K. Saha, D. F. Moyano and V. M. Rotello, *Mater. Horiz.*, 2013, **1**, 102–105.

16 B. D. Chithrani, A. A. Ghazani and W. C. W. Chan, *Nano Lett.*, 2006, **6**, 662–668.

17 B. Peter, N. Kanyo, K. D. Kovacs, V. Kovács, I. Szekacs, B. Pécz, K. Molnár, H. Nakanishi, I. Lagzi and R. Horvath, *ACS Appl. Bio Mater.*, 2023, **6**, 64–73.

18 D. Cheng, X. Li, G. Zhang and H. Shi, *Nanoscale Res Lett*, 2014, **9**, 195.

19 M. Siek, K. Kandere-Grzybowska and B. A. Grzybowski, *Acc. Mater. Res.*, 2020, **1**, 188–200.

20 M. Epple, V. M. Rotello and K. Dawson, *Acc. Chem. Res.*, 2023, **56**, 3369–3378.

21 A. Gupta, W. Ndugire, C.-M. Hirschbiegel, L. Grigely and V. M. Rotello, *Acc. Chem. Res.*, 2023, **56**, 2151–2169.

22 A. Verma, O. Uzun, Y. Hu, Y. Hu, H.-S. Han, N. Watson, S. Chen, D. J. Irvine and F. Stellacci, *Nature Mater*, 2008, **7**, 588–595.

23 Y.-S. S. Yang, P. U. Atukorale, K. D. Moynihan, A. Bekdemir, K. Rakhra, L. Tang, F. Stellacci and D. J. Irvine, *Nat Commun*, 2017, **8**, 14069.

24 P. Pengo, M. Şologan, L. Pasquato, F. Guida, S. Pacor, A. Tossi, F. Stellacci, D. Marson, S. Boccardo, S. Pricl and P. Posocco, *Eur Biophys J*, 2017, **46**, 749–771.

25 A. Chompoosor, K. Saha, P. S. Ghosh, D. J. Macarthy, O. R. Miranda, Z.-J. Zhu, K. F. Arcaro and V. M. Rotello, *Small*, 2010, **6**, 2246–2249.

26 Z.-J. Zhu, T. Posati, D. F. Moyano, R. Tang, B. Yan, R. W. Vachet and V. M. Rotello, *Small*, 2012, **8**, 2659–2663.

27 K. Saha, S. T. Kim, B. Yan, O. R. Miranda, F. S. Alfonso, D. Shlosman and V. M. Rotello, *Small*, 2013, **9**, 300–305.

28 A. K. Chew, B. C. Dallin and R. C. Van Lehn, *ACS Nano*, 2021, **15**, 4534–4545.

29 A. K. Chew, J. A. Pedersen and R. C. Van Lehn, *ACS Nano*, 2022, **16**, 6282–6292.

30 C. A. Huang-Zhu, J. K. Sheavly, A. K. Chew, S. J. Patel and R. C. Van Lehn, *ACS Nano*, 2024, **18**, 6424–6437.

31 C. A. Lochbaum, A. K. Chew, X. Zhang, V. Rotello, R. C. Van Lehn and J. A. Pedersen, *ACS Nano*, 2021, **15**, 6562–6572.

32 A. Marzouq, L. Morgenstein, C. A. Huang-Zhu, S. Yudovich, A. Atkins, A. Grupi, R. C. Van Lehn and S. Weiss, *Langmuir*, 2024, **40**, 10477–10485.

33 X. Zhang, G. Ma and W. Wei, *NPG Asia Mater*, 2021, **13**, 1–18.

34 G. Rossi and L. Monticelli, *Biochimica et Biophysica Acta (BBA) - Biomembranes*, 2016, **1858**, 2380–2389.

35 E. Canepa, S. Salassi, F. Simonelli, R. Ferrando, R. Rolandi, C. Lambruschini, F. Canepa, S. Dante, A. Relini and G. Rossi, *Sci Rep*, 2021, **11**, 1256.

36 R. C. Van Lehn, M. Ricci, P. H. J. Silva, P. Andreozzi, J. Reguera, K. Voïtchovsky, F. Stellacci and A. Alexander-Katz, *Nat Commun*, 2014, **5**, 4482.

37 F. Simonelli, D. Bochicchio, R. Ferrando and G. Rossi, *J. Phys. Chem. Lett.*, 2015, **6**, 3175–3179.

38 Y. Cao, J. Zhu, J. Kou, D. P. Tieleman and Q. Liang, *J. Chem. Theory Comput.*, 2024, **20**, 4045–4053.

39 Y. Oh and Q. Cui, *Nanoscale*, 2023, **15**, 12307–12318.

40 M. Wang, S.-D. Ni, Y.-W. Yin, Y.-Q. Ma and H.-M. Ding, *Langmuir*, 2024, **40**, 1295–1304.

41 X. Chen, D. P. Tieleman and Q. Liang, *Nanoscale*, 2018, **10**, 2481–2491.

42 S. Franco-Ulloa, D. Guarnieri, L. Riccardi, P. P. Pompa and M. De Vivo, *J. Chem. Theory Comput.*, 2021, **17**, 4512–4523.

43 M. Das, U. Dahal, O. Mesele, D. Liang and Q. Cui, *J. Phys. Chem. B*, 2019, **123**, 10547–10561.

44 F. Lolicato, L. Joly, H. Martinez-Seara, G. Fragneto, E. Scoppola, F. Baldelli Bombelli, I. Vattulainen, J. Akola and M. Maccarini, *Small*, 2019, **15**, 1805046.

45 H. Ding, W. Tian and Y. Ma, *ACS Nano*, 2012, **6**, 1230–1238.

46 L. Huang, Y. Yu, X. Lu, H. Ding and Y. Ma, *Nanoscale*, 2019, **11**, 2170–2178.

47 H. Nakamura, K. Sezawa, M. Hata, S. Ohsaki and S. Watano, *Phys. Chem. Chem. Phys.*, 2019, **21**, 18830–18838.

48 K. Shimizu, H. Nakamura and S. Watano, *Nanoscale*, 2016, **8**, 11897–11906.

49 Y. Ikeda, H. Nakamura, S. Ohsaki and S. Watano, *Phys. Chem. Chem. Phys.*, 2021, **23**, 10591–10599.

50 D. Nguyen, J. Wu, P. Corrigan and Y. Li, *Nanoscale*, 2023, **15**, 16112–16130.

51 Y.-Q. Chen, M.-D. Xue, J.-L. Li, D. Huo, H.-M. Ding and Y. Ma, *ACS Nano*, 2024, **18**, 6463–6476.

52 R. C. Van Lehn and A. Alexander-Katz, *PLOS ONE*, 2019, **14**, e0209492.

53 R. C. Van Lehn and A. Alexander-Katz, *J. Phys. Chem. A*, 2014, **118**, 5848–5856.

54 R. C. Van Lehn and A. Alexander-Katz, *Soft Matter*, 2015, **11**, 3165–3175.

55 J. K. Sheavly, J. A. Pedersen and R. C. Van Lehn, *Nanoscale*, 2019, **11**, 2767–2778.

56 J. K. Sheavly and R. C. Van Lehn, *AIChE Journal*, 2020, **66**, e16993.

57 P. Gkeka, P. Angelikopoulos, L. Sarkisov and Z. Cournia, *PLOS Computational Biology*, 2014, **10**, e1003917.

58 S. J. Patel and R. C. Van Lehn, *J. Phys. Chem. B*, 2021, **125**, 5862–5873.

59 A. C. Pan, D. Sezer and B. Roux, *J. Phys. Chem. B*, 2008, **112**, 3432–3440.

60 L. Maragliano, B. Roux and E. Vanden-Eijnden, *J. Chem. Theory Comput.*, 2014, **10**, 524–533.

61 D. Branduardi, F. L. Gervasio and M. Parrinello, *The Journal of Chemical Physics*, 2007, **126**, 054103.

62 A. K. Ghose and G. M. Crippen, *J. Chem. Inf. Comput. Sci.*, 1987, **27**, 21–35.

63 W. Humphrey, A. Dalke and K. Schulten, *Journal of Molecular Graphics*, 1996, **14**, 33–38.

64 R. C. Van Lehn and A. Alexander-Katz, *J. Phys. Chem. B*, 2014, **118**, 12586–12598.

65 S. Salassi, F. Simonelli, D. Bochicchio, R. Ferrando and G. Rossi, *J. Phys. Chem. C*, 2017, **121**, 10927–10935.

66 R. Patil, S. Das, A. Stanley, L. Yadav, A. Sudhakar and A. K. Varma, *PLOS ONE*, 2010, **5**, e12029.

67 J. Payandeh and M. Volgraf, *Nat Rev Drug Discov*, 2021, **20**, 710–722.

68 F. Eisenhaber, P. Lijnzaad, P. Argos, C. Sander and M. Scharf, *Journal of Computational Chemistry*, 1995, **16**, 273–284.

69 O. Elimelech, O. Aviv, M. Oded, X. Peng, D. Harries and U. Banin, *ACS Nano*, 2022, **16**, 4308–4321.

70 S. Yamashita, Y. Ito, H. Kamiya and Y. Okada, *Advanced Powder Technology*, 2024, **35**, 104277.

71 S. Ito, Y. Nakagawa, S. Yazawa, Y. Sasaki and S. Yajima, *Bioorganic & Medicinal Chemistry Letters*, 2014, **24**, 1812–1814.

72 K. Hashiba, Y. Sato, M. Taguchi, S. Sakamoto, A. Otsu, Y. Maeda, T. Shishido, M. Murakawa, A. Okazaki and H. Harashima, *Small Science*, 2023, **3**, 2200071.

73 D. Kim, D. W. Kim, H.-K. Lim, J. Jeon, H. Kim, H.-T. Jung and H. Lee, *Phys. Chem. Chem. Phys.*, 2014, **16**, 22717–22722.

74 W. Shinoda, M. Mikami, T. Baba and M. Hato, *J. Phys. Chem. B*, 2003, **107**, 14030–14035.

75 D. Van Der Spoel, E. Lindahl, B. Hess, G. Groenhof, A. E. Mark and H. J. C. Berendsen, *Journal of Computational Chemistry*, 2005, **26**, 1701–1718.

76 G. A. Tribello, M. Bonomi, D. Branduardi, C. Camilloni and G. Bussi, *Computer Physics Communications*, 2014, **185**, 604–613.

77 H. M. Khan, P. C. T. Souza, S. Thallmair, J. Barnoud, A. H. de Vries, S. J. Marrink and N. Reuter, *J. Chem. Theory Comput.*, 2020, **16**, 2550–2560.

78 D. H. de Jong, G. Singh, W. F. D. Bennett, C. Arnarez, T. A. Wassenaar, L. V. Schäfer, X. Periole, D. P. Tieleman and S. J. Marrink, *J. Chem. Theory Comput.*, 2013, **9**, 687–697.

79 S. O. Yesylevskyy, L. V. Schäfer, D. Sengupta and S. J. Marrink, *PLOS Computational Biology*, 2010, **6**, e1000810.

80 J. Michalowsky, L. V. Schäfer, C. Holm and J. Smiatek, *The Journal of Chemical Physics*, 2017, **146**, 054501.

81 T. A. Wassenaar, H. I. Ingólfsson, R. A. Böckmann, D. P. Tieleman and S. J. Marrink, *J. Chem. Theory Comput.*, 2015, **11**, 2144–2155.

82 F. Grunewald, G. Rossi, A. H. de Vries, S. J. Marrink and L. Monticelli, *J. Phys. Chem. B*, 2018, **122**, 7436–7449.

83 J. Huang and A. D. MacKerell Jr, *Journal of Computational Chemistry*, 2013, **34**, 2135–2145.

84. A. Grossfield, *WHAM: The Weighted Histogram Analysis Method, 2.0.11*, Grossfield Lab, Rochester, NY, 2013.